

# CHEMISTRY

## A European Journal

A Journal of



### Accepted Article

**Title:** 2D Metal-Organic Framework derived CuCo Alloy Nanoparticles Encapsulated Nitrogen-doped Carbonaceous Nanoleaves for Efficient Bifunctional Oxygen Electrocatalyst and Zinc-Air Batteries

**Authors:** Meiling Huo, Bin Wang, Chaochao Zhang, Shuping Ding, Haitao Yuan, Zuozhong Liang, Jing Qi, Mingxing Chen, Yang Xu, Wei Zhang, Haoquan Zheng, and Rui Cao

This manuscript has been accepted after peer review and appears as an Accepted Article online prior to editing, proofing, and formal publication of the final Version of Record (VoR). This work is currently citable by using the Digital Object Identifier (DOI) given below. The VoR will be published online in Early View as soon as possible and may be different to this Accepted Article as a result of editing. Readers should obtain the VoR from the journal website shown below when it is published to ensure accuracy of information. The authors are responsible for the content of this Accepted Article.

**To be cited as:** *Chem. Eur. J.* 10.1002/chem.201902389

**Link to VoR:** <http://dx.doi.org/10.1002/chem.201902389>

Supported by  
**ACES**

WILEY-VCH

DOI: 10.1002/((please add manuscript number))

Article type: Full Paper

**2D Metal-Organic Framework derived CuCo Alloy Nanoparticles Encapsulated Nitrogen-doped Carbonaceous Nanoleaves for Efficient Bifunctional Oxygen Electrocatalyst and Zinc-Air Batteries.**

*Meiling Huo,<sup>†, [a]</sup> Bin Wang,<sup>†, [a]</sup> Chaochao Zhang<sup>[a]</sup> Shuping Ding,<sup>[a]</sup> Haitao Yuan,<sup>[a]</sup> Zuozhong Liang,<sup>[a]</sup> Jing Qi,<sup>[a]</sup> Mingxing Chen,<sup>[a]</sup> Yang Xu,<sup>[a]</sup> Wei Zhang,<sup>[a]</sup> Haoquan Zheng,<sup>\*[a]</sup> and Rui Cao<sup>\*[a]</sup>*

[a] M. L. Huo, Dr. B. Wang, C. C. Zhang, S. P. Ding, H. T. Yuan, Z. Z. Liang, J. Qi, M. X. Chen, Y. Xu, Prof. Dr. W. Zhang, Prof. Dr. H. Q. Zheng, Prof. Dr. R. Cao  
Key Laboratory of Applied Surface and Colloid Chemistry, Ministry of Education,  
School of Chemistry and Chemical Engineering, Shaanxi Normal University, Xi'an  
710119, China. E-mail: ruicao@ruc.edu.cn; zhenghaoquan@snnu.edu.cn

<sup>†</sup> These authors contributed equally to this work.

**Keywords:** Metal-organic framework, CuCo alloy nanoparticle, nitrogen-doped carbon, oxygen electrocatalyst, zinc-air batteries

**Abstract:**

The development of efficient bifunctional electrocatalysts for oxygen reduction reaction (ORR) and oxygen evolution reaction (OER) is still remained a challenge in wide range of renewable energy technologies. Herein, CuCo alloy nanoparticles encapsulated nitrogen-doped carbonaceous nanoleaves (CuCo-NC) have been synthesized from a Cu(OH)<sub>2</sub>/2D leaf-like zeolitic imidazolate framework (ZIF-L)-pyrolysis approach. Leaf-like Cu(OH)<sub>2</sub> is first prepared by the ultra-sound induced self-assembly of Cu(OH)<sub>2</sub> nanowires. The efficient encapsulation of Cu(OH)<sub>2</sub> in ZIF-L is obtained due to the morphology fitting between the leaf-like Cu(OH)<sub>2</sub> and ZIF-L. CuCo-NC catalysts present superior electrocatalytic activity and stability toward ORR and OER over the commercial Pt/C and IrO<sub>2</sub>, respectively, which are further used as bifunctional oxygen electrocatalysts in Zn-air batteries and exhibits impressive performance, with a high peak power density of 303.7 mW cm<sup>-2</sup>, large specific capacity up to 751.4 mAh g<sup>-1</sup> at 20 mA cm<sup>-2</sup>, and a superior rechargeable stability.

## 1. Introduction

Rechargeable metal–air batteries have attracted great interest as a promising solution for energy-storage due to its high theoretical energy density, high security, and low cost.<sup>1-8</sup> Precious metal-based electrocatalysts have shown high activities for oxygen evolution reactions (OER) and oxygen reduction reactions (ORR). However, their poor stability and high cost limit the commercialization of metal–air batteries.<sup>9-19</sup> Therefore, developing efficient catalysts with low cost and electrocatalytic activity toward both OER and ORR is still one of the main challenges for metal–air batteries and other renewable energy technologies.<sup>20-33</sup>

The different electronegativity between carbon and nitrogen makes nitrogen-doped carbon (NC) materials potential electrocatalysts, which have been demonstrated to exhibit excellent catalytic properties.<sup>22, 34-41</sup> After encapsulating transition metals in N-doped carbons (M-NC), M-NC materials show enhanced electrocatalytic activities toward ORR/OER, which are attributed to the synergetic effects between the transition metal nanoparticles (NPs) and the NC shell.<sup>11, 34, 36, 42-54</sup> Compared to monometallic system, bimetallic or trimetallic alloys have shown promising catalytic activity, and sometimes unique catalytic activity, which monometallic systems do not have.<sup>11, 40, 55-62</sup> Among these systems, Cu based bimetallic alloy electrocatalysts attracted a lot of attentions, since Cu compounds exhibit biomimetic chemistry with O<sub>2</sub>.<sup>63-64</sup> However, Cu-based NC materials suffer from irreversible fusion and self-aggregation during pyrolysis at high-temperature, which is caused by its large diffusion constant at the same temperature.<sup>11, 65-67</sup> Therefore, it is still challenging to prepare Cu-based NC electrocatalysts with homogenous distribution of Cu species, which prevents the loss in electrocatalytic capabilities.

Zeolitic imidazolate frameworks (ZIFs) are a class of metal-organic frameworks, which have been considered as potential precursors for NC materials due to large surface areas and abundant N species.<sup>11, 68-74</sup> Recently, Zheng and co-workers reported that a Cu, Co@NC derived from ZIF-67 and Cu(OH)<sub>2</sub>. Instead of CuCo alloy nanoparticles, Cu and Co nanoparticles are separately but homogeneously distributed in NC framework.<sup>75</sup> More recently, Fe, Cu@NC was derived from ZIF-8 and used as electrocatalysts. Fe was homogeneously distributed throughout the entire architecture, while Cu was distributed in the form of dispersed nanoparticles throughout NC nanoparticle.<sup>76</sup> To date, it is still difficult to prepare a Cu based bimetallic alloy@NC based electrocatalysts for both ORR and OER.

Here, we fabricated a CuCo alloy NPs-encapsulated NC materials (CuCo@NC). ZIF-L-Co possesses a two-dimensional (2D) leaf-like morphology and a 2D layer-by-layer stacked structure as well. Guest molecules between the layers can be removed during pyrolysis.<sup>77-78</sup> Leaf-like Cu(OH)<sub>2</sub> has been synthesized by the ultra-sound induced self-assembly of Cu(OH)<sub>2</sub> nanowires. Thus, we propose that it is possible to fully confine the Cu species in this 2D layered framework, which prevents irreversible fusion that is commonly found in a three-dimensional (3D) continuous framework during pyrolysis. CuCo@NC exhibits superior OER and ORR bifunctional activity and impressive zinc-air performance. Specifically, when integrated into Zn-air batteries, a high peak power density of 303.7 mW cm<sup>-2</sup>, large specific capacity up to 751.4 mAh g<sup>-1</sup> at 20 mA cm<sup>-2</sup>, small charge-discharge voltage gap of about 0.84 V at 2 mA cm<sup>-2</sup>, and a superior rechargeable stability are observed, which is prominently superior to commercial Pt/C and Ir/C mixture catalyst.

## 2. Results and Discussion

### 2.1. Characterization of CuCo@NC electrocatalysts

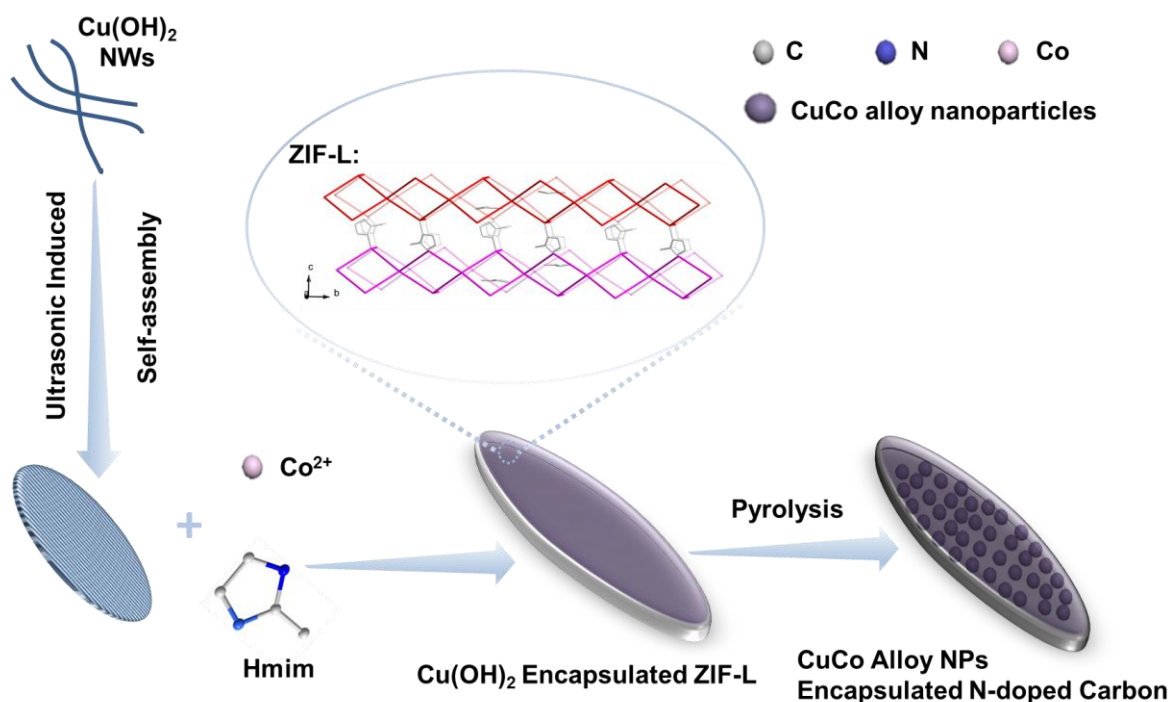


**Figure 1.** Schematic illustration of the preparation of CuCo@NC.

As illustrated in **Figure 1**, Cu(OH)<sub>2</sub> nanowires were first synthesized. Then, ultra-sound was used to induce the formation of leaf-like Cu(OH)<sub>2</sub> via self-assembly. Cu(OH)<sub>2</sub>@ZIF-L was synthesized by mixing pre-prepared Cu(OH)<sub>2</sub> with Co(NO<sub>3</sub>)<sub>2</sub> and 2-methylimidazole (Hmim) at ambient temperature. After pyrolysis at designed temperatures under argon (Ar) atmosphere, CuCo@NC was obtained. As shown in transmission electron microscopy (TEM) images, Cu(OH)<sub>2</sub> nanowires with 10 nm in diameter were successfully synthesized (Figure S1). When simply mixing the Cu(OH)<sub>2</sub> nanowires, Co(NO<sub>3</sub>)<sub>2</sub> and 2-methylimidazole, Cu(OH)<sub>2</sub> nanowires were not encapsulated in ZIF-L-Co. Instead, two separated phases, Cu(OH)<sub>2</sub> nanowires and ZIF-L-Co, were observed in the final product. Therefore, a further treatment of these nanowires in ultra-sound for 2 h was carried out. Leaf-like Cu(OH)<sub>2</sub> was formed *via* self-assembly (**Figure 2a**). As shown in Figure 2b, scanning electron microscopy (SEM) image shows that Cu(OH)<sub>2</sub>@ZIF-L-Co nanosheets display a leaf-like morphology, which is similar to that of traditional ZIF-L-Co nanosheets. The thickness of the leaf-like Cu(OH)<sub>2</sub>@ZIF-L-Co is approximately 450 nm, which is determined from the edge of the

material (Figure 2b, insert). After pyrolysis at 900 °C under Ar, the material keeps the leaf-like morphology, while its thickness decreases sharply to 180 nm (Figure 2c). There are pores, carbon nanotubes, and metal nanoparticles with size of 10-90 nm in the CuCo@NC framework (Figure 2d and 2e). As shown in the high-resolution TEM (Figure 2e), the metal nanoparticles were encapsulated in shelled NC multi-layered structure. The NC layers coated on metal nanoparticles prevent further aggregation from the formation of bigger nanoparticles. The interplanar distances of 0.36 nm and 0.208 nm from HRTEM image are indexed to the (002) plane of graphitic carbon and the (111) plane of Co, respectively.

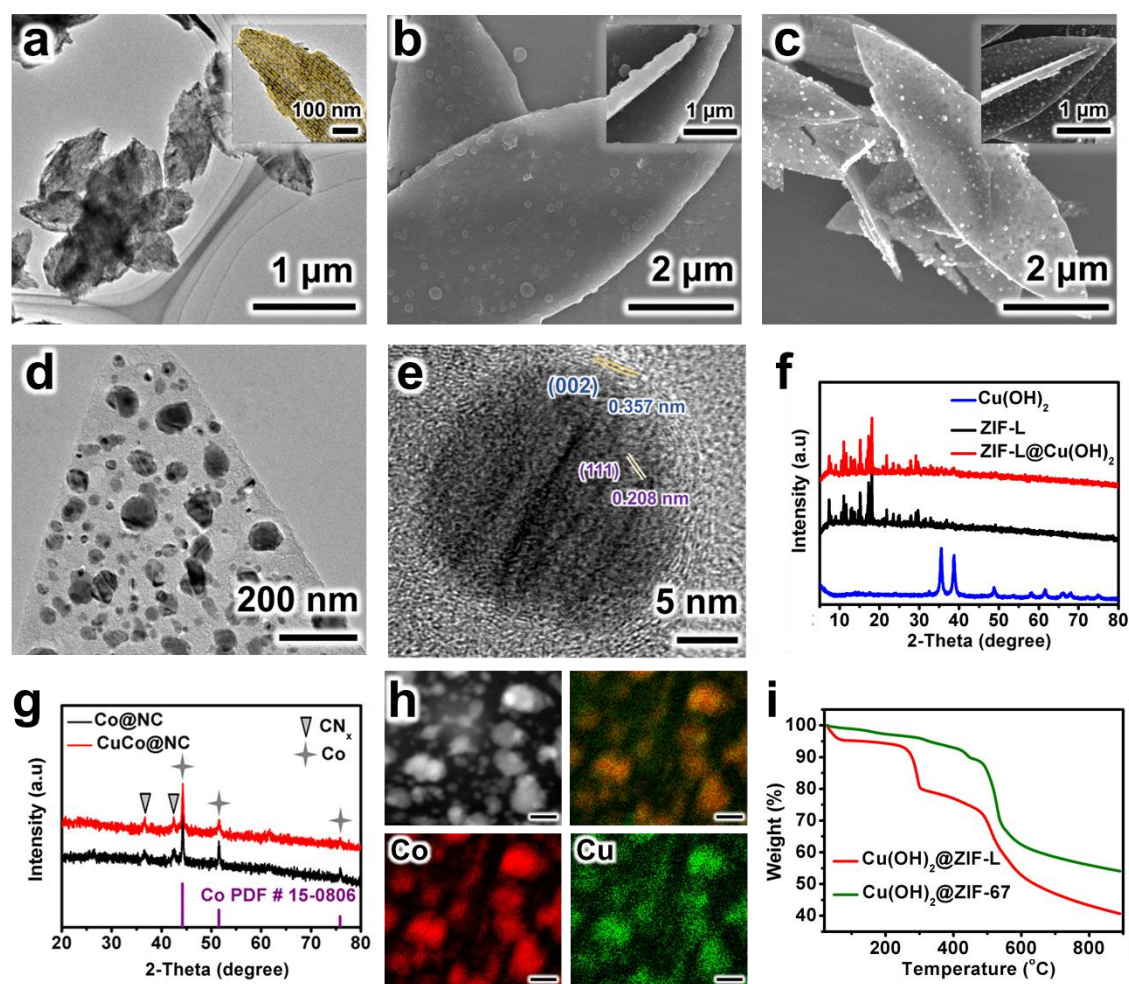


**Figure 2.** a) TEM image of leaf-like  $\text{Cu}(\text{OH})_2$ . b) SEM image of  $\text{Cu}(\text{OH})_2$ @ZIF-L. c) SEM image, d) TEM image and e) HRTEM image of CuCo@NC. f) XRD patterns of leaf-like  $\text{Cu}(\text{OH})_2$ , ZIF-L and  $\text{Cu}(\text{OH})_2$ @ZIF-L. g) XRD patterns of Co@NC and CuCo@NC. h) STEM and the corresponding EDS elemental mapping results of CuCo@NC. The scale bar in h) is 50 nm. i) Thermogravimetric analysis of  $\text{Cu}(\text{OH})_2$ @ZIF-L and  $\text{Cu}(\text{OH})_2$ @ZIF-67.

The powder X-ray diffraction (PXRD) pattern of  $\text{Cu}(\text{OH})_2@\text{ZIF-L-Co}$  shows diffraction peaks with high intensity, indicating the good crystallinity of the material and the formation of ZIF-L-Co (Figure 2f). The energy dispersive X-ray spectra (EDX) demonstrated that  $\text{Cu}(\text{OH})_2$  nanoleaves were well-scattered in ZIF-L nanosheets (Figure S2 and S3). PXRD pattern of  $\text{CuCo}@\text{NC}$  material has the same diffraction peaks as those of  $\text{Co}@\text{NC}$  (Figure 2g). We proposed that the Cu and Co formed CuCo alloy nanoparticles due to the similar unit cell and atomic arrangement of their face-centered-cubic (*fcc*) structure. As shown in high-angle annular dark field-scanning transmission electron microscopy (HAADF-STEM) image and the corresponding EDS mapping of  $\text{CuCo}@\text{NC}$ , the N element was homogeneously distributed throughout the whole nanoleaf (Figure S5), while Cu and Co were specifically located on the metal nanoparticles (Figure 2h). When zooming in an individual metal nanoparticle, Cu and Co elements were well-distributed, demonstrating the formation of CuCo alloy NPs. In the reported work using ZIF-67 instead of ZIF-L-Co, Cu and Co nanoparticles are separately but homogeneously distributed in NC framework derived from ZIF-67.<sup>75</sup> To further investigate the difference in ZIF-L-Co and ZIF-67 used in this system, thermogravimetric analyses (TG) of  $\text{Cu}(\text{OH})_2@\text{ZIF-L-Co}$  and  $\text{Cu}(\text{OH})_2@\text{ZIF-67}$  in  $\text{N}_2$  were performed (Figure 2i). Compared to ZIF-67, ZIF-L-Co has an extra weight loss at 250-300 °C, which was caused by the weight loss of Hmim between crystalline layered structure. The layered structure became dense after removal of these Hmim molecules at 450-500 °C, which happened before the decomposition of  $\text{Cu}(\text{OH})_2$ . Therefore, the Cu species were confined in nonporous 2D layered framework, which prevents irreversible fusion and give rise to the formation of CuCo alloy in the NC framework.

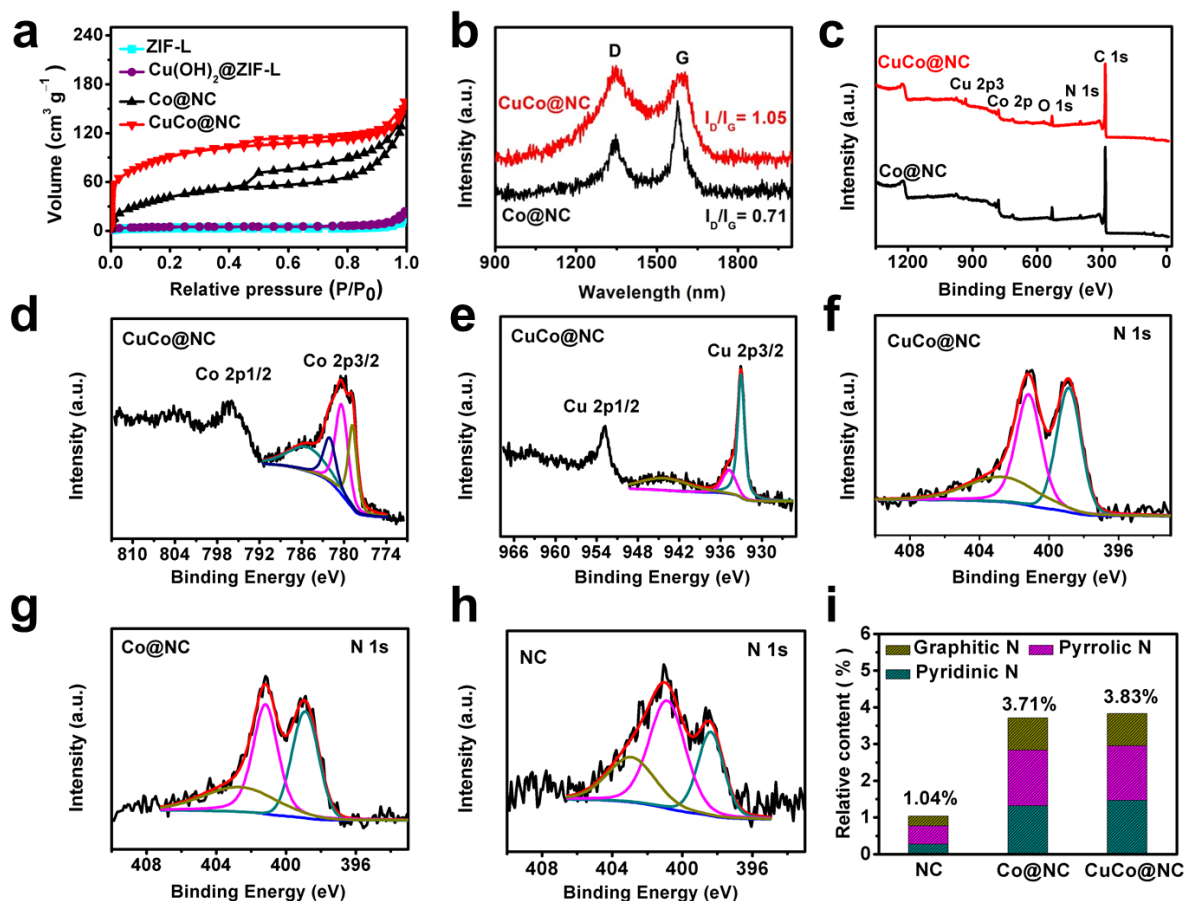


**Figure 3.** a)  $N_2$  adsorption/desorption isotherms of Co@NC, CuCo@NC and its corresponding precursors. b) Raman spectra of Co@NC and CuCo@NC. c) XPS survey spectra of Co@NC and CuCo@NC. High-resolution XPS spectra of d) Co 2p, e) Cu 2p, and f) N 1s of CuCo@NC composite. High-resolution XPS spectra of N 1s of g) Co@NC composite and h) NC composite. i) Different percentages of N species in CuCo@NC, Co@NC and NC.

$N_2$  adsorption/desorption isotherms of ZIF-L,  $Cu(OH)_2@ZIF-L$ , Co@NC, and CuCo@NC are shown in **Figure 3a**. The adsorption amounts of  $N_2$  in ZIF-L and  $Cu(OH)_2@ZIF-L$  are very low, indicating that both ZIF-L and  $Cu(OH)_2@ZIF-L$  possess no porous structure. This result can be explained by the layer-by-layer crystalline structure of ZIF-L, which is filled by Hmim molecules and has no space for the adsorption of  $N_2$  molecules. BET specific surface areas of Co@NC, and CuCo@NC after annealing are significantly higher than those of corresponding precursors. BET specific surface area of CuCo@NC ( $\sim 326 \text{ m}^2 \text{ g}^{-1}$ ) is more than twice comparable to that of the Co@NC ( $\sim 162 \text{ m}^2 \text{ g}^{-1}$ ). The introduction of  $Cu(OH)_2$  into ZIF-L causes the increased porosity of final CuCo@NC

product, which is favorable for mass transfer and beneficial for electrocatalysis. The characteristic G and D bands in the Raman spectra were located at 1600 and 1350  $\text{cm}^{-1}$ , respectively<sup>79</sup> (Figure 3b). The G band was assigned to the  $\text{sp}^2$  graphitic carbons, while the D band indicated the defective sites of disordered  $\text{sp}^3$  carbons in materials, which promoted electron transfer and provided more catalytic centers.<sup>80-83</sup> The intensity ratio between D and G bands ( $I_D/I_G$ ) of CuCo@NC was calculated to be 1.05, which was larger than that of Co@NC catalyst (0.71), indicating the formation of more defective carbons in CuCo@NC.

XPS measurements were further performed to analyze the surface chemical compositions of obtained samples. The survey spectra of CuCo@NC demonstrated the existence of C, N, Co, and Cu in CuCo@NC, indicating the doping of Cu element in CuCo@NC (Figure 3c). The XPS of CuCo@NC in Co  $2p_{3/2}$  region showed three main XPS peaks located at 778.8, 780.4, and 782.1 eV from the core photoelectron lines, which were assigned to the metallic Co,  $\text{CoO}_x/\text{CoC}_x\text{N}_y$ , and  $\text{CoN}_y$ , respectively (Figure 3d). Satellite peak of Co  $2p_{3/2}$  at 785.2 eV was observed, which was similar to those of Co@NC (Figure S6).<sup>75, 84-85</sup> In the high-resolution Cu  $2p_{3/2}$  XPS spectra of CuCo@NC, the peaks located at 933.0 and 934.7 eV were assigned to the Cu(0)/Cu(I) and Cu(II) species, respectively (Figure 3e). The Cu 2p satellite peak at 944.2 eV can be attributed to Cu(II) species in CuCo@NC due to unfilled electron state of Cu 3d9 orbitals.<sup>75, 86-87</sup>

The N contents in CuCo@NC, Co@NC, and NC are calculated to be 3.83, 3.71 and 1.04 at%, respectively, which are much higher than that in Co encapsulated N-doped carbon derived from ZIF-L.<sup>74</sup> NC was derived from ZIF-L-Zn at 900 °C in Ar, which has the same topological structure as ZIF-L-Co and is used as a reference. We further investigated the contents of different types of N in these materials (Figure 3f-i). The high-resolution N1s spectra of Co@NC and CuCo@NC are deconvoluted into three peaks, which are assigned to graphitic N (402.7 eV), pyrrolic N (401.2 eV) and pyridinic N (398.9 eV).<sup>88-89</sup> The

percentages of the different types of N in materials were calculated based on the integral areas of corresponding peaks (Figure 3i). CuCo@NC had the highest content of pyridinic N and graphitic N (2.6%) compared to that of Co@NC (2.1%) and NC (0.5%). The low content of NC may be attributed to the leaf-like morphology of NC, which gives rise to an easy loss of N at high temperature. As previously reported, the graphitic N and the pyridinic N are active sites for the ORR and OER.<sup>26, 28, 90-91</sup> Combining with Raman measurements, the addition of Cu(OH)<sub>2</sub> into ZIF-L-Co not only introduces Cu in CuCo alloy NPs but also gives rise to more defective sites in electrocatalysts, which are also expected to promote electron transfer and improve the electrocatalysis.

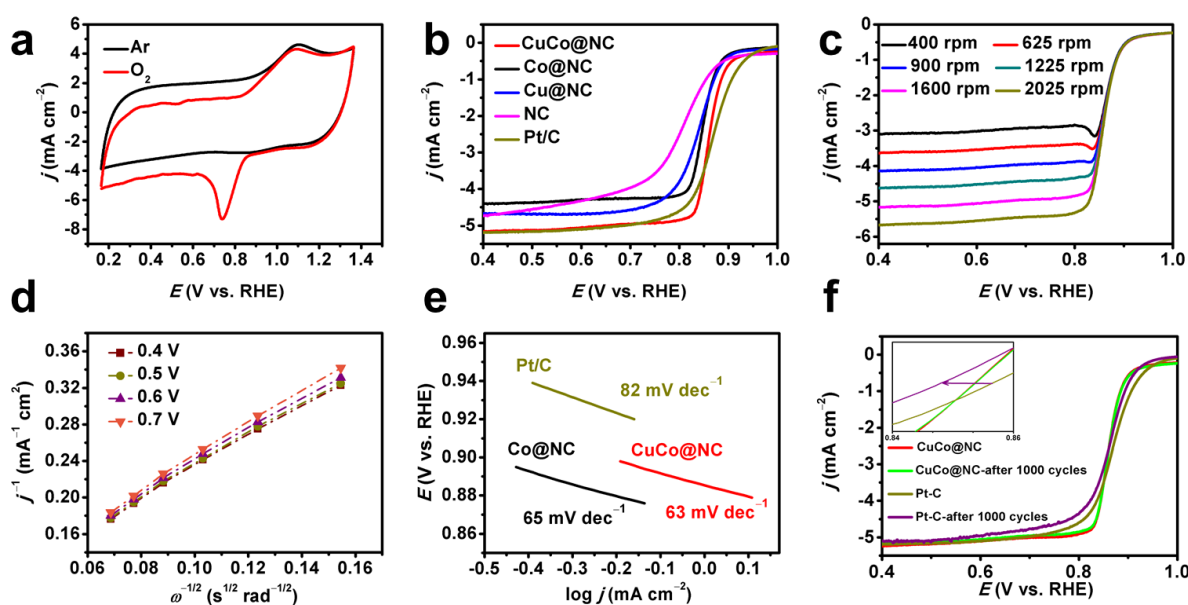


**Figure 4.** a) CV polarization curves of CuCo@NC in O<sub>2</sub>- or Ar-saturated 0.1 M KOH. b) LSV curves for the samples on an RDE at 1600 rpm in an O<sub>2</sub>-saturated 0.1 M KOH. c) LSV curves of CuCo@NC at different rotation speeds. d) Corresponding K-L plots of CuCo@NC at different potentials. e) Tafel slope values at low overpotential regions for CuCo@NC, Co@NC and Pt/C. f) LSV curves of CuCo@NC before and after 1000 cycles in O<sub>2</sub>-saturated 0.1 M KOH solution.

As bifunctional electrocatalysts for ORR and OER, the ORR electrocatalytic activity of CuCo@NC was first tested by cyclic voltammetry (CV) curves in O<sub>2</sub>-saturated 0.1 M KOH solution compared to that in Ar-saturated solution (**Figure 4a**). The CV of CuCo@NC shows

## WILEY-VCH

a stronger cathodic peak compared to that of Co@NC and Cu@NC (Figure S7), indicating its significantly efficient ORR performance. The doping amount of Cu(OH)<sub>2</sub> in ZIF-L-Co precursors would affect the state of Cu species, and the corresponding state of Co and the defective structure in the final CuCo-NC materials. The linear sweep voltammetry (LSV) polarization curves of CuCo@NC with different amounts of Cu(OH)<sub>2</sub> in ZIF-L-Co precursors were performed using a rotating disk electrode (RDE). The onset potential ( $E_{\text{onset}}$ ) and the half-wave potential ( $E_{1/2}$ ) of CuCo@NC increase with increasing Cu(OH)<sub>2</sub> contents in ZIF-L-Co and reach the highest values ( $E_{\text{onset}} = 0.945$  V,  $E_{1/2} = 0.866$  V) when doping 11 at% Cu(OH)<sub>2</sub> nanoleaves in ZIF-L-Co. When the Cu(OH)<sub>2</sub> doping further increases to 20 at%, their ORR activities decrease (Figure S8). The PXRD pattern of CuCo@NC with 20 at% Cu doping shows additional sharp diffraction peaks, which can be indexed as Cu nanoparticles instead of CuCo alloys (Figure S9). Therefore, the CuCo alloy structure is proposed to be important for the enhanced ORR performance.

The LSV curves for the NC, Cu@NC, Co@NC, CuCo@NC, and commercial Pt/C were then performed (Figure 4b). Among the non-precious metal catalysts, CuCo@NC exhibited the highest ORR activities ( $E_{\text{onset}} = 0.945$  V,  $E_{1/2} = 0.866$  V), which was higher than the NC, Co@NC and Cu@NC catalysts and comparable to Pt/C catalyst. Therefore, CuCo alloy NPs in NC is beneficial for the ORR performance, which is better than non-metal NC and monometallic NC. SEM images of Cu@NC, Co@NC, CuCo@NC after ORR performance tests show no significant change (Figure S10), indicating good structural stability of catalysts. The electrocatalysts synthesized by simply annealing physically mixed leaf-like Cu(OH)<sub>2</sub> and ZIF-L-Co showed a lower catalytic activity than CuCo@NC, indicating the importance of doping process (Figure S11). Polarization curves for CuCo@NC and Pt/C electrodes were recorded at rotation speeds from 400 to 2025 rpm (Figure 4c and S12). The Koutecky–Levich (K–L) plots from the kinetics diffusion control area exhibited a good parallelism and linearity, indicating the similar electron transfer number and the first order with respect to the

concentration of dissolved  $O_2$  at different potentials (Figure 4d).<sup>93-94</sup> The rotating ring-disk electrode (RRDE) technique was performed to investigate the mechanism. The electron transfer number for Co@NC and CuCo@NC catalysts are approaching the ideal value of 4.0, which are similar to that of the Pt/C (Figure S13 and S14). CuCo@NC had the smallest Tafel slope of  $63 \text{ mV dec}^{-1}$  (Figure 4e). The stability of catalyst was conducted with repetitive RDE voltammetry experiment. After 1000 cycles, the LSV of CuCo@NC catalyst is almost the same as that of initial state, while there is a decrease of  $E_{1/2}$  (10 mV) for Pt/C catalyst before and after 1000 cycles (Figure 4f). Compared with Pt/C catalyst, the CuCo@NC material exhibits higher resistance to the methanol cross-over effect in oxygen-saturated 0.1M KOH (Figure S15). Thus, CuCo@NC catalyst has superior stability.

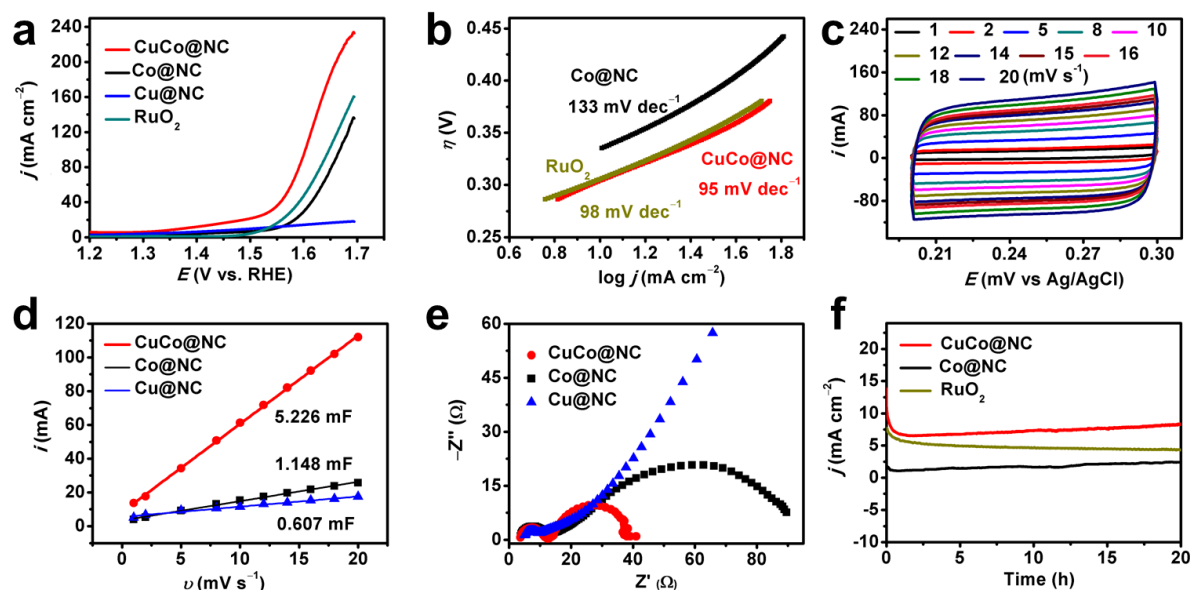


**Figure 5.** a) LSV curves of various samples for oxygen evolution in 1.0 M KOH solution. b) Tafel slopes for CuCo@NC, Co@NC, and RuO<sub>2</sub>. c) CV curves of CuCo@NC at various scan rates of in the range of 0.2-0.3 V vs. Ag/AgCl. d) Capacitance currents plotted versus scan rates of CuCo@NC, Co@NC, and Cu@NC. e) Impedance diagrams for CuCo@NC, Co@NC, and Cu@NC. f) Chronopotentiometry curves for CuCo@NC, Co@NC, and RuO<sub>2</sub>.

Subsequently, the OER tests of CuCo@NC, Cu@NC, Co@NC, and commercial RuO<sub>2</sub> were evaluated using a three-electrode system in 1 M KOH (Figure 5a). A potential of 1.568

V versus the reversible hydrogen electrode (vs. RHE) for CuCo@NC catalyst was needed to achieve a current density of  $50 \text{ mA cm}^{-2}$ . For the Co@NC catalyst and the state-of-art RuO<sub>2</sub>, higher potentials are needed to achieve a current density of  $50 \text{ mA cm}^{-2}$  (1.625 V vs. RHE for Co@NC and 1.603 V vs. RHE for the state-of-art RuO<sub>2</sub>) than that of CuCo@NC catalyst. The Tafel slope of CuCo@NC catalyst is the smallest ( $95 \text{ mV dec}^{-1}$ ) compared to that of Co@NC ( $133 \text{ mV dec}^{-1}$ ) and RuO<sub>2</sub> ( $98 \text{ mV dec}^{-1}$ ), confirming the superior electrochemical OER performance of CuCo@NC electrode (Figure 5b). The electrochemical surface area (ECSA) was calculated based on electrochemical double-layer capacitance ( $C_{dl}$ ) at the non-Faraday region (Figure 5c, 5d and S16).<sup>95</sup> The  $C_{dl}$  of CuCo@NC (5.226 mF) catalyst exhibited more than four times higher than that of Co@NC (1.148 mF) and Cu@NC (0.607 mF). The more exposed electrocatalytic active sites for OER lead to the superior catalytic performance of the CuCo@NC catalyst. The electrochemical impedance spectra of the electrocatalysts were shown in Figure 5e. As shown in impedance curves of CuCo@NC, Co@NC and Cu@NC, the second semicircles indicate that the CuCo@NC has the lowest charge transfer resistance among all electrocatalysts. The alloying of Co and Cu contributes to the increased electrical conductivity and further the enhanced activity of the CuCo@NC. Furthermore, the durability of the catalysts is essential to be measured. The chronopotentiometry curve of CuCo@NC showed no significant change during continuous electrolysis and attained a current density, which was higher than that of commercial RuO<sub>2</sub> and Co@NC, verifying excellent OER activity and its good stability (Figure 5f).

The superior ORR and OER performances of the CuCo@NC could be ascribed to the multiple synergistic effects. First, the presence of metallic Cu might favor the charge transport between the surface of the catalyst and the collector, thus endowing the catalyst with a high electrocatalytic activity. Second, the pyrolysis of Cu(OH)<sub>2</sub> in ZIF-L-Co at a high temperature caused the formation of more pores, which benefits the exposure of more electrochemical active sites. Third, benefiting from the unique 2D structure of the CuCo@NC and the alloy

forming of Cu and Co, the electrocatalytic activity might be remarkably promoted. Fourth, the graphitic N and the pyridinic N are active sites for the ORR and OER, which were coupled with defective sites certified by Raman spectra. Furthermore, the coordination between Co atoms and N atoms in N doped carbon could also tune the adsorption of the rate-determining intermediate (OOH\*), which is beneficial for the bifunctional electrocatalytic activity of the NC@Co nanocage catalysts toward ORR and OER.<sup>71</sup> All issues above endow the catalyst with a high electrocatalytic activity.

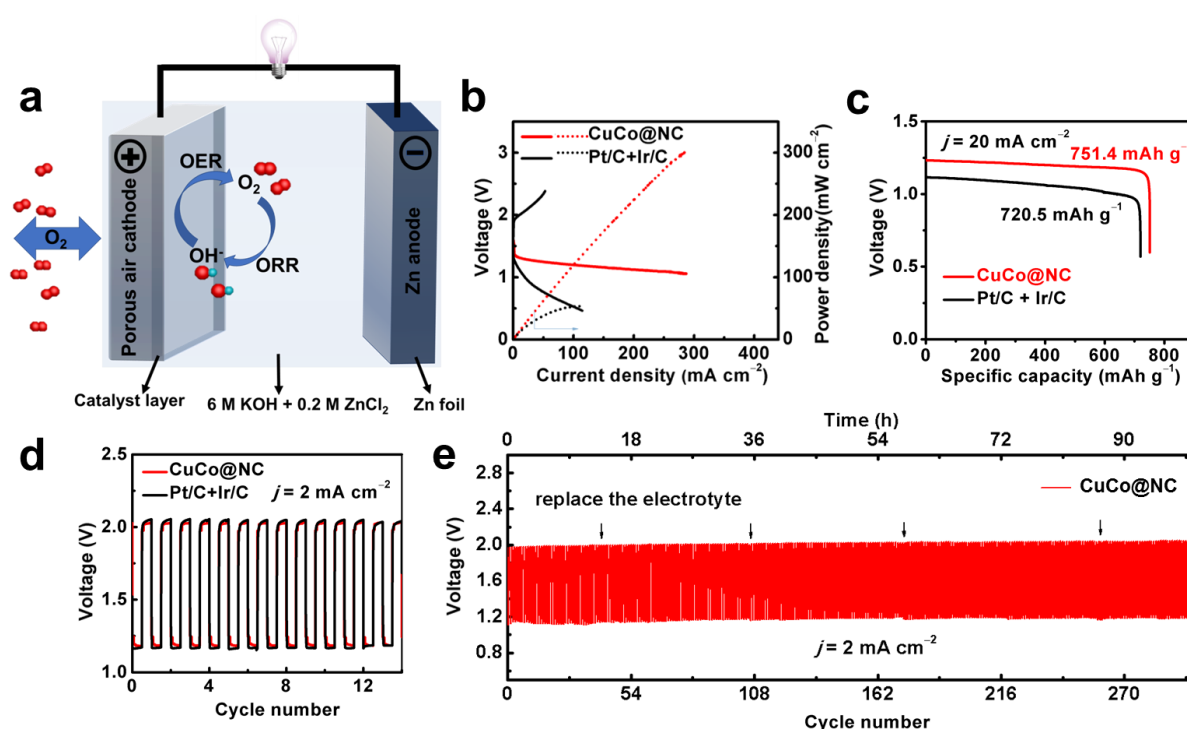


**Figure 6.** Application of bifunctional CuCo@NC in Zn-air batteries. a) The schematic of Zn-air batteries. b) Charge/discharge polarization and power density curves. c) Discharge curves at a constant current density of 20 mA cm<sup>-2</sup>. d) Charge-discharge cycling curves at 2 mA cm<sup>-2</sup>. e) Long cycling test.

The promising bifunctional performance of CuCo@NC makes it possible to construct rechargeable Zn-air batteries, which were further evaluated its application potentials. The anode was a Zn foil, while the air electrode was a catalyst-coated carbon cloth/gas diffusion layer, with a loading of 0.75 mg cm<sup>-2</sup> (Figure 6a). To ensure the reversible charge reactions

in anode, 0.2 M  $\text{ZnCl}_2$  was added in 6.0 M KOH as electrolyte. The mixture of Pt/C and Ir/C (1: 1 of mass ratio) was applied as a control sample for comparison.

The Zn-air battery catalyzed by CuCo@NC exhibits an evidently shrunken charge-discharge voltage gap compared to Pt/C + Ir/C (Figure 6b). Moreover, the peak power density of the one using CuCo@NC air electrode is  $303.7 \text{ mW cm}^{-2}$ , 6-times that of Pt/C + Ir/C, indicating a superior bifunctional activity and rechargeability. Notably, the Zn-air battery using CuCo@NC could be operated under extremely high current densities, with nearly  $300 \text{ mA cm}^{-2}$  for charge and over  $400 \text{ mA cm}^{-2}$  for discharge, which are obviously higher than the current densities of Pt/C + Ir/C ( $55.1$  and  $127.3 \text{ mA cm}^{-2}$  for charge and discharge, respectively). When galvanostatically discharging at  $20 \text{ mA cm}^{-2}$ , a considerably larger discharge voltage of around  $1.23 \text{ V}$  was delivered by the Zn-air battery based on CuCo@NC in comparison with Pt/C + Ir/C (Figure 6c). Moreover, no obvious degradation was observed. The specific capacity at  $20 \text{ mA cm}^{-2}$  for CuCo@NC based Zn-air battery is calculated to be  $751.4 \text{ mAh g}^{-1}$ , which is normalized to consumed Zn. It is higher than that of Pt/C + Ir/C ( $720.5 \text{ mAh g}^{-1}$ ) and corresponding to 91.6% of the theoretical value ( $820 \text{ mAh g}^{-1}$ ). All these metrics are one of the best results among reported non-precious-metal catalysts, and even superior to that of the commercial noble metal counterpart, revealing the superior bifunctional activity and rechargeability (Table S1).

Besides rechargeability, the stability of Zn-air batteries is critical for practical applications. When galvanostatically cycled at  $2 \text{ mA cm}^{-2}$ , a small charge-discharge voltage gap of about  $0.84 \text{ V}$  was detected for the Zn-air battery using CuCo@NC air electrode ( $1.19 \text{ V}$  for discharge and  $2.03 \text{ V}$  for charge), with a round-trip energy efficiency of 58% (Figure 6d). The voltage gap is smaller than that of Pt/C + Ir/C and can be further decreased by around  $30 \text{ mV}$  after 14 cycle test, which is attributed to a surface activation of zinc anode during the dissolution/deposition process of the initial cycling. Furthermore, the Zn-air battery using

CuCo@NC exhibits a stable charge and discharge voltage throughout 100 h cycling test, revealing excellent stability (Figure 6e). The performance degradation during long time cycling is caused by the reaction of the alkaline electrolyte and CO<sub>2</sub> in atmosphere, which can be regenerated when refreshing electrolytes.

### 3. Conclusion

CuCo alloy nanoparticles encapsulated nitrogen-doped carbonaceous nanoleaves have been prepared by pyrolysis of a 2D leaf-like Cu(OH)<sub>2</sub>/ZIF-L material. The CuCo-NC catalysts present superior electrocatalytic activity and stability toward ORR and OER over the commercial Pt/C and IrO<sub>2</sub>, respectively. The high efficiency of the CuCo-NC catalysts in both ORR and OER is attributed to the synergistic effects of CuCo alloy, high surface area and high N content. The constructed Zn-air battery using CuCo-NC catalysts showed impressive performance, with a peak power density of 303.7 mW cm<sup>-2</sup>, a large specific capacity of 751.4 mAh g<sup>-1</sup> at 20 mA cm<sup>-2</sup>, a small charge-discharge voltage gap of about 0.84 V at 2 mA cm<sup>-2</sup>, and a good rechargeable stability. This work opens up new opportunities for design and construction of bifunctional oxygen electrocatalysts using a 2D leaf-like Cu(OH)<sub>2</sub>/ZIF-L material for energy conversion and storage applications.

### 4. Experimental Section

*Methods and materials:* Co(NO<sub>3</sub>)<sub>2</sub>·6H<sub>2</sub>O (99.99%), CuCl<sub>2</sub> (99%), and Hmim (98%) were purchased from the Energy Chemical. NaOH (98%) was purchased from Sinopharm Group Chemical Reagent Co., Ltd. Polyethylene glycol (M<sub>w</sub>= 20000) was purchased from Tianjin Kemiou Chemical Reagent Co., Ltd. All chemicals were used without further purification.

*Synthesis of leaf-like Cu(OH)<sub>2</sub>:* Cu(OH)<sub>2</sub> nanowires were synthesized as precursors. In a typical synthesis condition, 180 mg of copper chloride (CuCl<sub>2</sub>) and 200 mg of polyethylene

glycol ( $M_w = 20000$ ) were dissolved in 200 mL of deionized water under stirring. Then 1.2 mL of deionized water containing 288 mg of sodium hydroxide was added dropwise into the above solution. The mixed solution was kept at room temperature for 30 min under stirring. The obtained  $\text{Cu}(\text{OH})_2$  nanowires were centrifuged (10000 rpm, 5 min), washed with deionized water for several times, and finally dried in vacuum freeze dryer. Then, leaf-like  $\text{Cu}(\text{OH})_2$  was prepared using the synthetic ratio of per 50 mg of  $\text{Cu}(\text{OH})_2$  nanowires dispersed in 10 mL deionized water under ultrasonication for 2 h.

*Synthesis of  $\text{Cu}(\text{OH})_2@ZIF-L$  nanosheets:* Typically,  $\text{Cu}(\text{OH})_2$  nanoleaves (12.5-100 mg) and  $\text{Co}(\text{NO}_3)_2 \cdot 6\text{H}_2\text{O}$  (0.58 g) were mixed in 40 mL of deionized water, then sonicated for 30 min at room temperature. Afterwards, 40 mL of deionized water containing 1.3 g of Hmim was added into the above solution under stirring. The mixture was stirred at room temperature for 4 h. The obtained purple precipitates were collected by centrifugation (10000 rpm, 5 min), washed with methanol for several times, and dried in vacuum freeze dryer for further application. The composite without adding  $\text{Cu}(\text{OH})_2$  nanoleaves was prepared by a procedure similar to that for preparing  $\text{Cu}(\text{OH})_2@ZIF-L$  nanosheets.

*Synthesis of  $\text{CuCo}@NC$  nanosheets:* The quartz boat containing  $\text{Cu}(\text{OH})_2@ZIF-L$  (200 mg) powders was placed in a tube furnace under Ar flow without heating for 30 min to remove air. Carbonization of the composite was performed under Ar at 900 °C for 2 h with a heating ramp of 5 °C·min<sup>-1</sup>. Furthermore, all comparative samples, such as Co@NC, NC, m-CuCoNC and m-CuNC were pyrolyzed under the same program (900 °C for 2 h).

*Electrochemical studies:* A CHI 760E Electrochemical Analyzer (CH Instruments) and a Pine Modulated Speed Rotator (Pine Research Instrumentation, Inc.) were used to carry out all electrochemical experiments of ORR performance at ambient temperature. Typically, all electrochemical measurements were carried out in a 0.1 M KOH solution and performed with a three-electrode configuration, using a RDE (area of 0.196 cm<sup>2</sup>) or a RRDE (area of 0.247

cm<sup>2</sup>) electrode as the working electrode, a Pt wire as the counter electrode, and an saturated Ag/AgCl as the reference electrode. All potentials converted into RHE with the conversion  $E(\text{vs. RHE}) = E(\text{vs. Ag/AgCl}) + 0.197 \text{ V} + 0.059 \times \text{pH}$ .

For the fabrication of the working electrode, 5 mg of the catalyst was dispersed in 450  $\mu\text{L}$  of isopropanol, 20  $\mu\text{L}$  of deionized water and 10  $\mu\text{L}$  of 5 wt% Nafion aqueous solution. The mixed solution was sonicated for 1h to form a homogeneous suspension. Then 20  $\mu\text{L}$  of the catalysts was drop-casted onto the RDE electrode (catalyst loading:  $\sim 0.4 \text{ mg cm}^{-2}$ ) and dried naturally to form a homogeneous membrane. For the ORR, before the measurement, use Ar/O<sub>2</sub> flow to bubble the electrolyte at least 30 minutes. The electrochemical experiments were conducted in O<sub>2</sub>-saturated 0.1 M KOH for ORR. The CV experiments were carried out electrolyte solutions with a scan rate of 10 mV s<sup>-1</sup> at room temperature. The LSV of RDE measurements were performed at various rotating rate from 400 to 2025 rpm with a scan rate of 5 mV s<sup>-1</sup>. RRDE measurements were performed with a scan rate of 5 mV s<sup>-1</sup> at room temperature and the ring-electron potential was set to 1.5 V vs RHE. The electron transferred number ( $n$ ) and the hydrogen peroxide yield (H<sub>2</sub>O<sub>2</sub> %) can be calculated according to the following formulas:

$$H_2O_2(\%) = 200 \times \frac{\frac{I_r}{N}}{I_d + \frac{I_r}{N}}$$

$$n = 4 \times \frac{I_d}{I_d + \frac{I_r}{N}}$$

$I_d$  is the disk current;  $I_r$  is the ring current;  $N$  is the current collection efficiency of the Pt ring ( $\sim 0.39$  with the LSV measurement in K<sub>3</sub>Fe[CN]<sub>6</sub> solution).

For OER, all electrochemical measurements were performed with a three-electrode configuration and carried out in a 1.0 M KOH solution at room temperature. A glassy carbon (GC, area of 0.07 cm<sup>2</sup>) electrode, a Pt wire, and an saturated Ag/AgCl were used as the

working electrode, as the auxiliary electrode, and as the reference electrode, respectively. Typically, 2 mg of the catalyst was added in 30  $\mu\text{L}$  of the Nafion solution (5 wt%, DuPont) and suspended in 1 mL of water–ethanol solution (vol. ratio of 2: 1). The solution was sonicated for 1 h to form a homogeneous slurry. Afterwards, 5  $\mu\text{L}$  of the as-prepared catalysts were loaded onto a GC electrode. The Tafel plots were measured by carrying out the LSV at a scanning rate of 5  $\text{mV s}^{-1}$ .

For Zn-air battery, a polished Zn foil with thickness of 0.25 mm, 6.0 M KOH solution (containing 0.2 M  $\text{ZnCl}_2$ ), catalyst-coated carbon cloth/gas diffusion layer (CC/GDL) were used as anode, as electrolyte, and as air electrode, respectively. The carbon cloth (1.5  $\times$  1.5  $\text{cm}^2$ , WOS 1009, CeTech) was attached on GDL through a hot-press method. Then a certain volume of catalyst ink was dropped on CC/GDL to reach a catalyst loading of 0.75  $\text{mg cm}^{-2}$ .

### Supporting Information

Supporting Information is available from the Wiley Online Library or from the author.

### Acknowledgements

We are grateful for support from the “Thousand Talents Program” of China, the National Natural Science Foundation of China (Grant Nos. 21601118, 21101170, 21573139, and 21773146), the Fundamental Research Funds for the Central Universities (GK201903033), and the Research Funds of Shaanxi Normal University.

Received: ((will be filled in by the editorial staff))

Revised: ((will be filled in by the editorial staff))

Published online: ((will be filled in by the editorial staff))

### References

- 1 J.-S. Lee, S. Tai Kim, R. Cao, N.-S. Choi, M. Liu, K. T. Lee, J. Cho, *Adv. Energy Mater.* **2011**, 1, 34.
- 2 F. Cheng, J. Chen, *Chem. Soc. Rev.* **2012**, 41, 2172.

- 3 Y. Li, M. Gong, Y. Liang, J. Feng, J. E. Kim, H. Wang, G. Hong, B. Zhang, H. Dai, *Nat. Commun.* **2013**, 4, 1805.
- 4 D. Yu, K. Goh, H. Wang, L. Wei, W. Jiang, Q. Zhang, L. Dai, Y. Chen, *Nat. Nanotech.* **2014**, 9, 555.
- 5 F. Meng, H. Zhong, D. Bao, J. Yan, X.-B. Zhang, *J. Am. Chem. Soc.* **2016**, 138, 10226.
- 6 S. S. Shinde, C. H. Lee, A. Sami, D. H. Kim, S. U. Lee, J. H. Lee, *ACS Nano* **2017**, 11, 347.
- 7 D. Yang, L. Zhang, X. Yan, X. Yao, *Small Methods* **2017**, 1, 1700209.
- 8 D. Guan, J. Meng, D. M. Reiner, N. Zhang, Y. Shan, Z. Mi, S. Shao, Z. Liu, Q. Zhang, S. J. Davis, *Nat. Geosci.* **2018**, 11, 551.
- 9 Y. Zheng, Y. Jiao, M. Jaroniec, Y. Jin, S. Z. Qiao, *Small* **2012**, 8, 3550.
- 10 J. Tian, Q. Liu, N. Cheng, A. M. Asiri, X. Sun, *Angew. Chem. Int. Ed.* **2014**, 53, 9731.
- 11 C. Yuan, H. B. Wu, Y. Xie, X. W. Lou, *Angew. Chem. Int. Ed.* **2014**, 53, 1488.
- 12 L. Bu, S. Guo, X. Zhang, X. Shen, D. Su, G. Lu, X. Zhu, J. Yao, J. Guo, X. Huang, *Nat. Commun.* **2016**, 7, 11850.
- 13 W. Xiao, W. Lei, M. Gong, H. L. Xin, D. Wang, *ACS Catal.* **2018**, 8, 3237.
- 14 L. Yang, X. Zeng, W. Wang, D. Cao, *Adv. Funct. Mater.* **2018**, 28, 1704537.
- 15 D. Chen, M. Qiao, Y.-R. Lu, L. Hao, D. Liu, C.-L. Dong, Y. Li, S. Wang, *Angew. Chem. Int. Ed.* **2018**, 57, 8691.
- 16 T. Liu, M. Zhang, Y. L. Wang, Q. Y. Wang, C. Lv, K. X. Liu, S. Suresh, Y. H. Yin, Y. Y. Hu, Y. S. Li, X. B. Liu, S. W. Zhong, B. Y. Xia, Z. P. Wu, *Adv. Energy Mater.* **2018**, 8, 1802349.
- 17 B.-Q. Li, S.-Y. Zhang, L. Kong, H.-J. Peng, Q. Zhang, *Adv. Mater.* **2018**, 30, 1870160.
- 18 J. Tang, N. Qin, Y. Chong, Y. Diao, Yiliguma, Z. Wang, T. Xue, M. Jiang, J. Zhang, G. Zheng, *Nat. Commun.* **2018**, 9, 786.

- 19 F. L. Meng, Z. L. Wang, H. X. Zhong, J. Wang, J. M. Yan, X.-B. Zhang, *Adv. Mater.* **2016**, 28, 7948.
- 20 M. W. Kanan, D. G. Nocera, *Science* **2008**, 321, 1072.
- 21 G. Wu, P. Zelenay, *Acc. Chem. Res.* **2013**, 46, 1878.
- 22 W. He, C. Jiang, J. Wang, L. Lu, *Angew. Chem. Int. Ed.* **2014**, 53, 9503.
- 23 N. T. Suen, S. F. Hung, Q. Quan, N. Zhang, Y. J. Xu, H. M. Chen, *Chem. Soc. Rev.* **2017**, 46, 337.
- 24 S. Wan, J. Qi, W. Zhang, W. Wang, S. Zhang, K. Liu, H. Zheng, J. Sun, S. Wang, R. Cao, *Adv. Mater.* **2017**, 29, 1700286.
- 25 M. Borghei, J. Lehtonen, L. Liu, O. J. Rojas, *Adv. Mater.* **2018**, 30, 1703691.
- 26 S. Han, X. Hu, J. Wang, X. Fang, Y. Zhu, *Adv. Energy Mater.* **2018**, 8, 1800955.
- 27 J. Qi, W. Zhang, R. Cao, *Adv. Energy Mater.* **2018**, 8, 1701620.
- 28 A. Sarapuu, E. Kibena-Pöldsepp, M. Borghei, K. Tammeveski, *J. Mater. Chem. A* **2018**, 6, 776.
- 29 P. Han, Z. Wang, M. Kuang, Y. Wang, J. Liu, L. Hu, L. Qian, G. Zheng, *Adv. Energy Mater.* **2018**, 8, 1870112.
- 30 Y.-H. Zhu, X. Yang, X.-B. Zhang, *Angew. Chem. Int. Ed.* **2017**, 56, 6378.
- 31 Y.-H. Zhu, Y.-B. Yin, X. Yang, T. Sun, S. Wang, Y.-S. Jiang, J.-M. Yan, X.-B. Zhang, *Angew. Chem. Int. Ed.* **2017**, 56, 7881.
- 32 B. Wang, C. Tang, H.-F. Wang, X. Chen, R. Cao, Q. Zhang, *Adv. Mater.* **2019**, 31, 1805658.
- 33 B. Wang, C. Tang, H.-F. Wang, B.-Q. Li, X. Cui, Q. Zhang, *Small Methods* **2018**, 2, 1800055.
- 34 J. Masa, W. Xia, M. Muhler, W. Schuhmann, *Angew. Chem. Int. Ed.* **2015**, 54, 10102.
- 35 H. Yu, L. Shang, T. Bian, R. Shi, G. I. N. Waterhouse, Y. Zhao, C. Zhou, L.-Z. Wu, C.-H. Tung, T. Zhang, *Adv. Mater.* **2016**, 28, 5080.

- 36 C. Zhu, H. Li, S. Fu, D. Du, Y. Lin, *Chem. Soc. Rev.* **2016**, 45, 517.
- 37 C. Hu, L. Dai, *Adv. Mater.* **2017**, 29, 1604942.
- 38 J. Zhu, Y. Huang, W. Mei, C. Zhao, C. Zhang, J. Zhang, I. S. Amiinu, S. Mu, *Angew. Chem. Int. Ed.* **2019**, 58, 3859.
- 39 H. Li, N. Cheng, Y. Zheng, X. Zhang, H. Lv, D. He, M. Pan, F. Kleitz, S. Z. Qiao, S. Mu, *Adv. Energy Mater.* **2013**, 3, 1176.
- 40 K. Gao, B. Wang, L. Tao, B. V. Cunning, Z. Zhang, S. Wang, R. S. Ruoff, L. Qu, *Adv. Mater.* **2018**, 31, 1805121.
- 41 C. Tang, H.-F. Wang, X. Chen, B.-Q. Li, T.-Z. Hou, B. Zhang, Q. Zhang, M.-M. Titirici, F. Wei, *Adv. Mater.* **2016**, 28, 6845.
- 42 L. Han, S. Dong, E. Wang, *Adv. Mater.* **2016**, 28, 9266.
- 43 K. Shen, X. Chen, J. Chen, Y. Li, *ACS Catal.* **2016**, 6, 5887.
- 44 W. Xia, A. Mahmood, Z. Liang, R. Zou, S. Guo, *Angew. Chem. Int. Ed.* **2016**, 55, 2650.
- 45 M. Zhou, H.-L. Wang, S. Guo, *Chem. Soc. Rev.* **2016**, 45, 1273.
- 46 J. Nai, Y. Lu, L. Yu, X. Wang, X. W. Lou, *Adv. Mater.* **2017**, 29, 1703870.
- 47 Z. W. Seh, J. Kibsgaard, C. F. Dickens, I. Chorkendorff, J. K. Nørskov, T. F. Jaramillo, *Science* **2017**, 355.
- 48 W. Zhang, W. Lai, R. Cao, *Chem. Rev.* **2017**, 117, 3717.
- 49 Y. Zheng, Y. Jiao, Y. Zhu, Q. Cai, A. Vasileff, L. H. Li, Y. Han, Y. Chen, S.-Z. Qiao, *J. Am. Chem. Soc.* **2017**, 139, 3336.
- 50 Y. P. Zhu, C. Guo, Y. Zheng, S.-Z. Qiao, *Acc. Chem. Res.* **2017**, 50, 915.
- 51 X. Li, H. Lei, J. Liu, X. Zhao, S. Ding, Z. Zhang, X. Tao, W. Zhang, W. Wang, X. Zheng, R. Cao, *Angew. Chem. Int. Ed.* **2018**, 57, 15070.
- 52 Z. Lu, B. Wang, Y. Hu, W. Liu, Y. Zhao, R. Yang, Z. Li, J. Luo, B. Chi, Z. Jiang, M. Li, S. Mu, S. Liao, J. Zhang, X. Sun, *Angew. Chem. Int. Ed.* **2019**, 131, 2648.

- 53 H. Lv, Z. Xi, Z. Chen, S. Guo, Y. Yu, W. Zhu, Q. Li, X. Zhang, M. Pan, G. Lu, S. Mu, S. Sun, *J. Am. Chem. Soc.* **2015**, 137, 5859.
- 54 F. Meng, H. Zhong, D. Bao, J. Yan, X.-B. Zhang, *J. Am. Chem. Soc.* **2016**, 138, 10226.
- 55 G. Nam, J. Park, M. Choi, P. Oh, S. Park, M. G. Kim, N. Park, J. Cho, J.-S. Lee, *ACS Nano* **2015**, 9, 6493.
- 56 Y. Yang, Z. Lun, G. Xia, F. Zheng, M. He, Q. Chen, *Energy Environ. Sci.* **2015**, 8, 3563.
- 57 V. R. Calderone, N. R. Shiju, D. C. Ferré, G. Rothenberg, *Green Chem.* **2011**, 13, 1950.
- 58 K. Xiao, X. Qi, Z. Bao, X. Wang, L. Zhong, K. Fang, M. Lin, Y. Sun, *Catal. Sci. Technol.* **2013**, 3, 1591.
- 59 G. Prieto, S. Beijer, M. L. Smith, M. He, Y. Au, Z. Wang, D. A. Bruce, K. P. de Jong, J. J. Spivey, P. E. de Jongh, *Angew. Chem. Int. Ed.* **2014**, 53, 6397.
- 60 A. Cao, G. Liu, Y. Yue, L. Zhang, Y. Liu, *RSC Adv.* **2015**, 5, 58804.
- 61 W. Gao, Y. Zhao, H. Chen, H. Chen, Y. Li, S. He, Y. Zhang, M. Wei, D. G. Evans, X. Duan, *Green Chem.* **2015**, 17, 1525.
- 62 Y. Chen, Q. L. Zhu, N. Tsumori, Q. Xu, *J. Am. Chem. Soc.* **2015**, 137, 106.
- 63 M. Jahan, Z. Liu, K. P. Loh, *Adv. Funct. Mater.* **2013**, 23, 5363.
- 64 S.-K. Lee, S. D. George, W. E. Antholine, B. Hedman, K. O. Hodgson, E. I. Solomon, *J. Am. Chem. Soc.* **2002**, 124, 6180.
- 65 J. Wang, K. Wang, F. B. Wang, X. H. Xia, *Nat. Commun.* **2014**, 5, 5285.
- 66 H. Yu, A. Fisher, D. Cheng, D. Cao, *ACS Appl. Mater. Interfaces* **2016**, 8, 21431.
- 67 Y. Liu, Y. Han, Z. Zhang, W. Zhang, W. Lai, Y. Wang, R. Cao, *Chem. Sci.* **2019**, 10, 2613.
- 68 Z. Yang, Y. Xia, R. Mokaya, *J. Am. Chem. Soc.* **2007**, 129, 1673.
- 69 H. B. Wu, B. Y. Xia, L. Yu, X. Y. Yu, X. W. Lou, *Nat. Commun.* **2015**, 6, 6512.

- 70 P. Yin, T. Yao, Y. Wu, L. Zheng, Y. Lin, W. Liu, H. Ju, J. Zhu, X. Hong, Z. Deng, G. Zhou, S. Wei, Y. Li, *Angew. Chem. Int. Ed.* **2016**, 55, 10800.
- 71 S. Liu, Z. Wang, S. Zhou, F. Yu, M. Yu, C. Y. Chiang, W. Zhou, J. Zhao, J. Qiu, *Adv. Mater.* **2017**, 29, 1700874.
- 72 J. Meng, C. Niu, L. Xu, J. Li, X. Liu, X. Wang, Y. Wu, X. Xu, W. Chen, Q. Li, Z. Zhu, D. Zhao, L. Mai, *J. Am. Chem. Soc.* **2017**, 139, 8212.
- 73 J. Wang, Z. Huang, W. Liu, C. Chang, H. Tang, Z. Li, W. Chen, C. Jia, T. Yao, S. Wei, Y. Wu, Y. Li, *J. Am. Chem. Soc.* **2017**, 139, 17281.
- 74 Z. Liang, C. Zhang, H. Yuan, W. Zhang, H. Zheng, R. Cao, *Chem. Commun.* **2018**, 54, 7519.
- 75 M. Kuang, Q. Wang, P. Han, G. Zheng, *Adv. Energy Mater.* **2017**, 7, 1700193.
- 76 Z. Wang, H. Jin, T. Meng, K. Liao, W. Meng, J. Yang, D. He, Y. Xiong, S. Mu, *Adv. Funct. Mater.* **2018**, 28, 1802596.
- 77 R. Chen, J. Yao, Q. Gu, S. Smeets, C. Baerlocher, H. Gu, D. Zhu, W. Morris, O. M. Yaghi, H. Wang, *Chem. Commun.* **2013**, 49, 9500.
- 78 Z. Zhong, J. Yao, Z.-X. Low, R. Chen, M. He, H. Wang, *Carbon* **2014**, 72, 242.
- 79 S. Wang, X.-B. Zhang, *Adv. Mater.* **2019**, 31, 1805432.
- 80 M. Chen, J. Qi, D. Guo, H. Lei, W. Zhang, R. Cao, *Chem. Commun.* **2017**, 53, 9566.
- 81 Y. Li, B. Jia, Y. Fan, K. Zhu, G. Li, C.-Y. Su, *Adv. Energy Mater.* **2018**, 8, 1702048.
- 82 Z. Liang, X. Fan, H. Lei, J. Qi, Y. Li, J. Gao, M. Huo, H. Yuan, W. Zhang, H. Lin, H. Zheng, R. Cao, *Angew. Chem. Int. Ed.* **2018**, 57, 13187.
- 83 J. Tang, R. R. Salunkhe, J. Liu, N. L. Torad, M. Imura, S. Furukawa, Y. Yamauchi, *J. Am. Chem. Soc.* **2015**, 137, 1572.
- 84 Z. Li, M. Shao, L. Zhou, R. Zhang, C. Zhang, M. Wei, D. G. Evans, X. Duan, *Adv. Mater.* **2016**, 28, 2337.

- 85 T. Palaniselvam, V. Kashyap, S. N. Bhange, J.-B. Baek, S. Kurungot, *Adv. Funct. Mater.* **2016**, 26, 2150.
- 86 B. Voloskiy, H. Fei, Z. Zhao, S. Lee, M. Li, Z. Lin, B. Papandrea, C. Wang, Y. Huang, X. Duan, *ACS Appl. Mater. Interfaces* **2016**, 8, 26769.
- 87 H. Wu, H. Li, X. Zhao, Q. Liu, J. Wang, J. Xiao, S. Xie, R. Si, F. Yang, S. Miao, X. Guo, G. Wang, X. Bao, *Energy Environ. Sci.* **2016**, 9, 3736.
- 88 B. Liu, L. Jin, H. Zheng, H. Yao, Y. Wu, A. Lopes, J. He, *ACS Appl. Mater. Interfaces* **2017**, 9, 1746.
- 89 Q. L. Zhu, W. Xia, T. Akita, R. Zou, Q. Xu, *Adv. Mater.* **2016**, 28, 6391.
- 90 L. Lai, J. R. Potts, D. Zhan, L. Wang, C. K. Poh, C. Tang, H. Gong, Z. Shen, J. Lin, R. S. Ruoff, *Energy Environ. Sci.* **2012**, 5, 7936.
- 91 Z. D. Yang, X. Y. Yang, T. Liu, Z. W. Chang, Y. B. Yin, X.-b. Zhang, J. M. Yan, Q. Jiang, *Small* **2018**, 14, 1800590.
- 92 L. Kong, J. Zhu, W. Shuang, X.-H. Bu, *Adv. Energy Mater.* **2018**, 8, 1801515.
- 93 S. Guo, S. Zhang, S. Sun, *Angew. Chem. Int. Ed.* **2013**, 52, 8526.
- 94 A. Aijaz, N. Fujiwara, Q. Xu, *J. Am. Chem. Soc.* **2014**, 136, 6790.
- 95 H. Liang, F. Meng, M. Caban-Acevedo, L. Li, A. Forticaux, L. Xiu, Z. Wang, S. Jin, *Nano Lett.* **2015**, 15, 1421.

WILEY-VCH

## 2D Metal-Organic Framework derived CuCo Alloy Nanoparticles Encapsulated Nitrogen-doped Carbonaceous Nanoleaves for Efficient Bifunctional Oxygen Electrocatalyst and Zinc-Air Batteries.

**Keyword:** metal-organic framework, CuCo alloy nanoparticle, nitrogen-doped carbon, oxygen electrocatalyst, zinc-air batteries.

M. L. Huo, B. Wang, C. C. Zhang, S. P. Ding, H. T. Yuan, Z. Z. Liang, J. Qi, M. M. Chen, Y. Xu, W. Zhang, H. Q. Zheng,<sup>\*</sup> and R. Cao<sup>\*</sup>

